



Microstructure Evolution and Mechanical Properties of Friction Stir Welded Al–Cu–Li Alloy

Peng Chen^{1,2,3} · Wenhao Chen¹ · Jiaxin Chen³ · Zhiyu Chen¹ · Yang Tang⁴ · Ge Liu⁵ · Bensheng Huang^{1,2} · Zhiqing Zhang³

Received: 28 October 2023 / Revised: 15 December 2023 / Accepted: 1 January 2024 / Published online: 5 March 2024
© The Chinese Society for Metals (CSM) and Springer-Verlag GmbH Germany, part of Springer Nature 2024

Abstract

The investigation concentrates on friction stir welded (FSW) Al–Cu–Li alloy concerning its local microstructural evolution and mechanical properties. The grain features were characterized by electron back scattered diffraction (EBSD) technology, while precipitate characterization was conducted by using transmission electron microscopy (TEM) aligned along $[011]_{\text{Al}}$ and $[001]_{\text{Al}}$ zone axes. The mechanical properties are evaluated through micro-hardness and tensile testing. It can be found that nugget zones exhibit finely equiaxed grains evolved through complete dynamic recrystallization (DRX), primarily occurring in continuous dynamic recrystallization (CDRX) and discontinuous dynamic recrystallization (DDRX). In the thermal–mechanically affected zone (TMAZ), numerous sub-structured grains, exhibiting an elongated morphology, were created due to partial DRX, signifying the dominance of CDRX, DDRX, and geometric dynamic recrystallization (GDRX) in this region. T_1 completely dissolves in the nugget zone (NZ) leading to the formation of Guinier–Preston zones and increase of δ' , β' and S' . Conversely, T_1 partially solubilizes in TMAZ, the lowest hardness zone (LHZ) and heat affected zone (HAZ), and the residual T_1 undergoes marked coarsening, revealing various T_1 variants. The solubilization and coarsening of T_1 are primary contributors to the degradation of hardness and strength. θ' primarily dissolves and coarsens in NZ and TMAZ, whilst this precipitate largely coarsens in HAZ and LHZ. σ , T_B , grain boundary phases (GBPs) and precipitate-free zone (PFZ) are newly generated during FSW. σ exists in the TMAZ, LHZ and HAZ, whereas T_B nucleates in NZ. GBPs and PFZ mostly develop in LHZ and HAZ, which can cause strain localization during tensile deformation, potentially leading to LHZ joint fracture.

Keywords Al–Cu–Li alloy · Friction stir welding · Microstructure evolution · Mechanical properties

Available online at <http://link.springer.com/journal/40195>.

✉ Peng Chen
xd_chenpeng@163.com

✉ Bensheng Huang
hbslxp@163.com

✉ Zhiqing Zhang
zqzhang@cqu.edu.cn

³ College of Materials Science and Engineering, Chongqing University, Chongqing 400045, China

⁴ School of Mechatronic Engineering, Southwest Petroleum University, Chengdu 610500, China

⁵ School of Robot Engineering, Yangtze Normal University, Chongqing 408100, China

¹ School of New Energy and Materials, Southwest Petroleum University, Chengdu 610500, China

² Sichuan Provincial Engineering Research Center of Advanced Materials Manufacturing Technology for Shale Gas High-Efficient Exploitation, Southwest Petroleum University, Chengdu 610500, China

1 Introduction

As a kind of primary aerospace structural material, Al–Cu–Li alloy successfully combines low density with high strength [1, 2]. Currently, this alloy contributes up to 8.8% of the structure weight in the C919's large plane, contributing to a 7% weight reduction of the aircraft, significantly reducing operating expenditure [3]. The usage of Al–Cu–Li alloy into aerospace vehicles reflects the industry's superior production level [4]. In the actual production, the manufacturing of supersize Al–Cu–Li alloy overall structure has become a key technological breakthrough, and efficient joining process is the challenge for this high-strength Al alloy [5, 6]. Friction stir welding (FSW), a kind of solid-phase connection technology, typically generates at 0.6–0.9 T_m (T_m is melting temperature in Kelvin), commendably avoiding most fusion welding drawbacks [7]. Consequently, it is deemed as an optimal choice for welding Al–Cu–Li alloy, with numerous related studies being conducted [5–10].

Most of the studies are focused on the effect of welding parameters on microstructure and mechanical properties of Al–Cu–Li alloy FSW joints [2]. Welding process windows for this alloy in different chemical component and plate thickness have been obtained, yielding enhanced FSW joint mechanical properties [5]. The discussion has encompassed material flow, welding heat cycle and microstructure evolution during FSW [5, 6]. Furthermore, the studies about microstructure evolution in FSW joints mainly involve in dynamic recrystallization (DRX) for grains as well as precipitation behavior for phases [11, 12]. Complete DRX is observed in the nugget zone (NZ), whereas partial DRX occurs in the thermal-mechanically affected zone (TMAZ) [13]. Heat affected zone (HAZ) mainly experiences recovery, indicating little change in grain morphology and size [11]. Different DRX mechanisms are identified within the different regions of FSW joints, signifying the presence of continuous dynamic recrystallization (CDRX), discontinuous dynamic recrystallization (DDRX), and geometric

dynamic recrystallization (GDRX) in addition to partial DRX [14].

Al–Cu–Li alloy represents a typical precipitation-strengthening aluminum alloy, with properties mainly governed by precipitates. T_1 (Al_2CuLi), the predominant strengthening precipitate, has received significant attention. Shen et al. reports that T_1 mostly dissolves in NZ and TMAZ, while significantly coarsens in HAZ [15]. However, Chen et al. reveals that T_1 is mainly dissolved in TMAZ I, while coarsened in TMAZ II [16]. In addition, the researchers have also revealed that this precipitate is completely dissolved in the NZ, but can re-precipitate at the top of NZ with elevated rotation speeds [17]. Besides, the development of θ' (Al_2Cu), δ' (Al_3Li), β' (Al_3Zr) and T_B ($Al_{7.5}Cu_4Li$) in Al–Cu–Li alloy FSW joints, relating to dissolution, coarsening, precipitation and re-precipitation behavior, is noted [18–20]. Nevertheless, transmission electron microscopy (TEM) characterization, typically performed along one diffraction direction, leaves some precipitate data unexplored [15, 21–23]. Therefore, evolution mechanisms of precipitate in Al–Cu–Li alloy FSW joints are still not clear.

Al–Cu–Li alloy has complex precipitate systems, including Guinier–Preston zones (GPZs), T_1 , θ' , δ' , β' , T_B , S' (Al_2CuMg), T_2 (Al_6CuLi), and possibly σ (Al_5Cu_6Mg) and T ($Al_{20}Cu_2Mn_3$) as well [29]. The common precipitates are summarized in Table 1. T_1 is the most important strengthening precipitate in this alloy, which always nucleates on the (111) plane of Al matrix and develops four variants. This precipitate has a platelet shape and is viewed with various morphologies along different directions, indicating a plate by front view and needle-like by side view [30]. Thus, under TEM inspection, variations in T_1 morphologies become apparent depending on the diffraction direction, illustrated in Fig. 1. With a $[011]_{Al}$ zone axis diffraction, two variants of T_1 ($T_1^{(1\#)}$ and $T_1^{(3\#)}$) often display needle-like shapes, whereas the remaining variants are difficult to observe [31]. Upon significant coarsening, however, the two variants ($T_1^{(2\#)}$ and $T_1^{(4\#)}$) take on elliptical shapes as observed in TEM [32]. While all four variants cannot be identified along a $[001]_{Al}$ zone axis diffraction unless severely coarsened

Table 1 Main precipitates in Al–Cu–Li alloy [22, 24–28]

Phase	Crystal structure	Lattice constant (nm)			Orientation relationship	Morphology
		<i>a</i>	<i>b</i>	<i>c</i>		
T_1	Hexagonal	0.497		0.935	$(0001)_{T_1} \parallel (111)_{Al}$ $[101]_{T_1} \parallel [-110]_{Al}$	Plate
δ'	$L1_2$	0.401–0.404			$(111)_{\delta'} \parallel (111)_{Al}$	Spherical
β'	$L1_2$	0.405			$(111)_{\beta'} \parallel (111)_{Al}$	Spherical
θ'	Tetragonal	0.404–0.408		0.58	$[001]_{\theta'} \parallel [100]_{Al}$	Plate
S'	Orthorhombic	0.404	0.925	0.718	$[100]_{S'} \parallel [100]_{Al}$ $[010]_{S'} \parallel [02-1]_{Al}$ $[001]_{S'} \parallel [012]_{Al}$	Lath, rod
T_B	CaF_2	0.583		0.58	$[001]_{T_B} \parallel [100]_{Al}$	Rod
σ	Cubic	0.829			$(100)_{\sigma} \parallel (100)_{Al}$ $[100]_{\sigma} \parallel [100]_{Al}$	Cubical

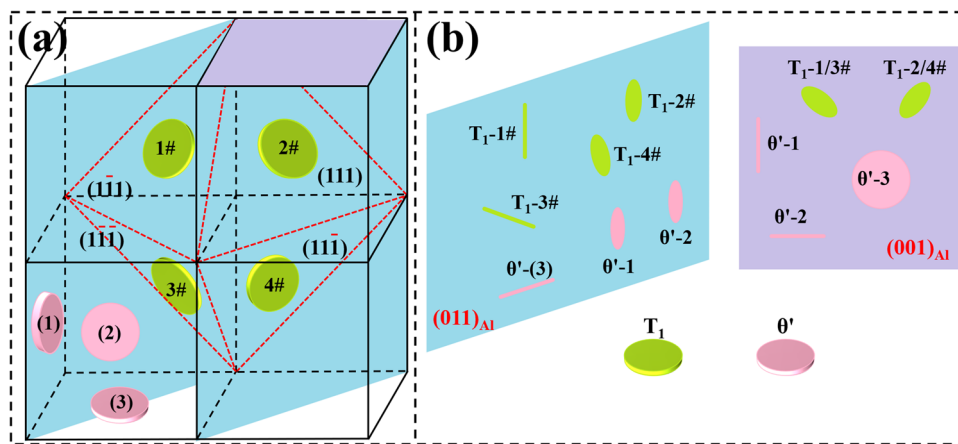


Fig. 1 T_1 is marked green; θ' is marked pink; $(011)_{Al}$ plane is marked blue; $(001)_{Al}$ plane is marked purple. Schematic diagram of **a** habit precipitation locations of T_1 and θ' , and **b** morphological features of T_1 and θ' along $[011]_{Al}$ and $[001]_{Al}$ zone axes

and in elliptic form [31]. The needle-like T_1 is frequently detected in Al–Cu–Li alloy FSW joints, however, the elliptical-like precipitate is seldom reported, resulting from lack of precipitate analysis in detail.

θ' , a common strengthening precipitate in 2xxx Al alloys, forms three variations on $(001)_{Al}$ habit planes [28], as shown in Fig. 1. The platelet-like θ' presents distinct slice orientations by TEM observation across diversified diffraction paths. When scanning $[011]_{Al}$ zone axis, one variant of θ' ($\theta'-3$), displays a needle shape, whereas non-observable unless distinctly coarsened into an elliptical shape [31]. However, when analyzing $[001]_{Al}$ zone axis, the two variants ($\theta'-1$ and $\theta'-2$) typically appear needle-shaped, making $\theta'-3$ challenging to ascertain unless it is visibly coarsened and visualizes as a disk. Therefore, θ' is more easily distinguished along $[001]_{Al}$ zone axis than $[011]_{Al}$ zone axis. Additionally, cubic σ has been discovered in the TMAZ along $[011]_{Al}$ zone axis [33], yet is visually clearer along $[001]_{Al}$ zone axis. S' can also be observed along the two diffraction directions, the morphological identification being facilitated along $[001]_{Al}$ zone axis [27]. Nevertheless, TEM characterization of Al–Cu–Li alloy FSW joints mostly relies on $[011]_{Al}$ zone axis, seldom considering alternative diffraction paths, potentially limiting the overall representation of these precipitates. Understanding precipitate evolution necessitates TEM analysis utilizing different diffraction paths.

FSW is a complicated thermo-mechanical process, causing marked variations in precipitate development, mainly involving in dissolution, coarsening and precipitation behavior across the adjacent regions of the joints [34]. Generally, softening of Al–Cu–Li alloy FSW joints is attributed to the dissolution and coarsening of strengthening precipitates [5]. Joint failure often occurs in the softest region which is usually called the lowest hardness

zone (LHZ) [34]. Fracture mechanism of the joints significantly depends on precipitates in LHZ. TEM samples of LHZ for precipitate characterization is always prepared by the conventional wire cutting and electrolytic double jet [18, 20, 22]. However, the LHZ is located at the boundary region between the HAZ and the TMAZ, a region so narrow that TEM observation of samples is challenging. This means that precipitate feature and evolution of LHZ is still unclear. Thus, a more precise technique to obtain LHZ samples is essential.

Consequently, in this paper, microstructure evolution and mechanical properties of Al–Cu–Li alloy FSW joints are studied, focusing on the discussion about DRX mechanism and precipitation behavior in different regions of the joints. To comprehend the precipitation characteristics in these regions, TEM observation is performed on $[011]_{Al}$ and $[001]_{Al}$ zone axes. In addition, focused ion beam (FIB) technology has been utilized for sample preparation of the LHZ. Based on the microstructure analysis, a correlation between microstructure and mechanical properties is established, thereby unveiling the joint fracture mechanism.

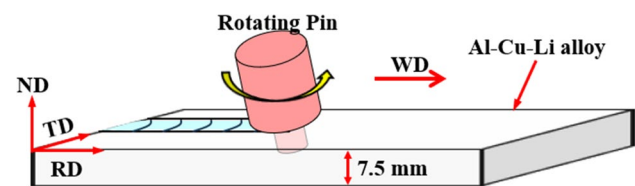


Fig. 2 Schematic diagram of Al–Cu–Li alloy FSW process

2 Materials and Methods

In this study, the base material (BM) is a 7.5 mm thick Al–Cu–Li alloy (4 wt% Cu, 1 wt% Li, 0.44 wt% Mg, 0.4 wt% Ag, 0.11 wt% Zr, 0.05 wt% Fe) plate with peak artificial aging temper conditions (solution heat-treating at 520 °C for 2 h + quenching in water + cold working by 3% deformation + artificial aging at 160 °C for 15 h).

The BM was subjected to friction stir butt welding with a rotation speed of 700 r/min and a welding speed of 50 mm/min. Welding direction (WD) was carried out along rolling direction (RD) of the BM with a shoulder plunge depth of 0.1 mm and a tool tilt angle of 2.5°, as shown in Fig. 2. FSW tool is made of high-speed steel and consists of a concave shoulder with 18 mm in diameter and a threaded taper cylindrical pin with 6.9 mm in length.

Microstructure characterization was conducted on the transverse cross-section of FSW joints, focusing on grain and precipitate features in different regions of the joints by electron back scattered diffraction (EBSD) and transmission electron microscopy (TEM) technologies. EBSD specimens were prepared by grinding and mechanical polishing, and then electro-polishing with a mixture of 10% HClO₄ and 90% C₂H₅OH for 120 s at 20 V and −20 °C. EBSD test was carried out by scanning electron microscopy (SEM, Zeiss Auriga) with an operating voltage of 20 kV, and the EBSD scanning step size was performed on 0.3 μm. EBSD data were processed by HKL Channel 5 software. TEM samples were prepared by two methods: one was by twin-jet electro-polishing with a solution of 70% CH₃OH and 30% HNO₃ at 15 V and −30 °C, and the other was by focused ion beam (FIB) technology using the Zeiss Auriga FIB-SEM. Precipitate characterization is carried out by combining scanning transmission electron microscopy-dark field (STEM-DF) and selected area electron diffraction (SAED) analysis using Thermo Scientific Talos F200S at 200 kV. Positions for TEM observation were marked in the Fig. 3, in which “a–d” are located at the NZ, TMAZ, LHZ and HAZ, respectively.

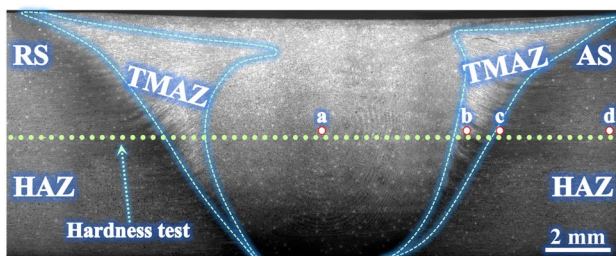


Fig. 3 Macroscopic morphology of the cross-section of Al–Cu–Li alloy FSW joints

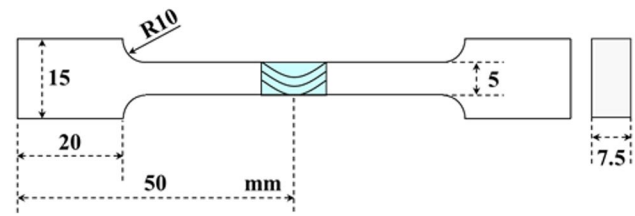


Fig. 4 Schematic diagram of the tensile test specimens

Hardness distribution was measured on the transverse cross-section of the joints by MH-5L micro-hardness testers. The measurement was carried out in the middle thickness of the joints with an interval of 0.5 mm under a load of 500 g for 10 s. Tensile test specimens were prepared as per ASTM: E8- M11 guidelines, and schematic diagram of the specimens was shown in Fig. 4. Room-temperature tensile tests were carried out using AG-X testing machines (maximum load of 50 kN, accuracy of $\pm 0.5\%$) with a displacement state of 1 mm/min, and three samples were tested for each condition. Fracture morphology was analyzed using Zeiss Auriga FIB-SEM. To explore the deformation behavior and failure mechanism, strain distribution of the joints during tensile deformation was analyzed by digital image correlation (DIC) technology.

3 Results

3.1 Hardness Profiles of the Joints

Hardness profiles of Al–Cu–Li alloy FSW joints are shown in Fig. 5. Hardness distribution of the joints exhibits a characteristic “W” shape, a definitive feature of precipitation-hardened Al alloy FSW joints. Compared with the BM,

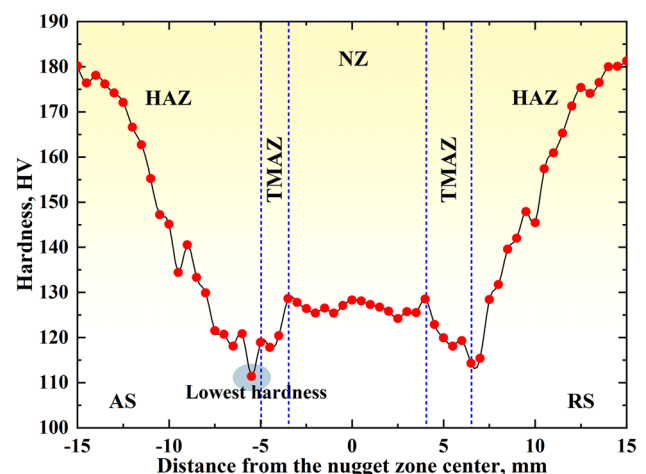


Fig. 5 Hardness profiles of Al–Cu–Li alloy FSW joints

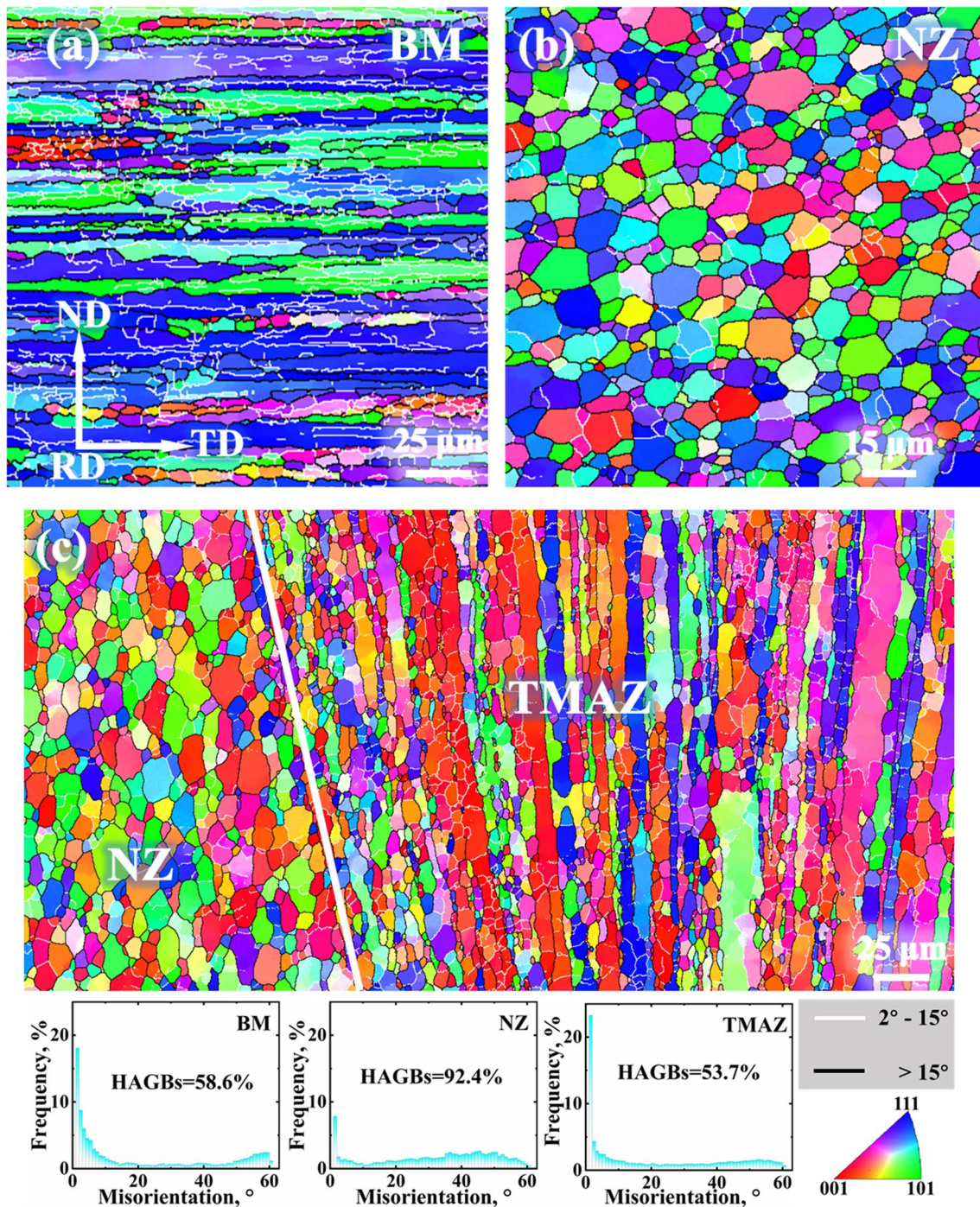


Fig. 6 EBSD analysis of **a** BM, **b** NZ, **c** NZ-TMAZ

hardness of the joints is obviously decreased. On each side of the weld, hardness firstly rises slightly within the NZ-TMAZ transition zone, before dropping steadily from TMAZ to HAZ and returning to BM levels post-HAZ. This results in the lowest hardness being located near the TMAZ–HAZ transition zone. This area is commonly denoted as LHZ, generally situated adjacent to the TMAZ in the HAZ [34].

3.2 Grain Features of the Joints

Grain morphology and crystallographic orientation features of BM, NZ and TMAZ are analyzed by EBSD, as shown in Fig. 6. Various colors appear in EBSD maps representing different crystallographic directions which can reference the IPF coloring scheme. Low angle grain boundaries (LAGBs),

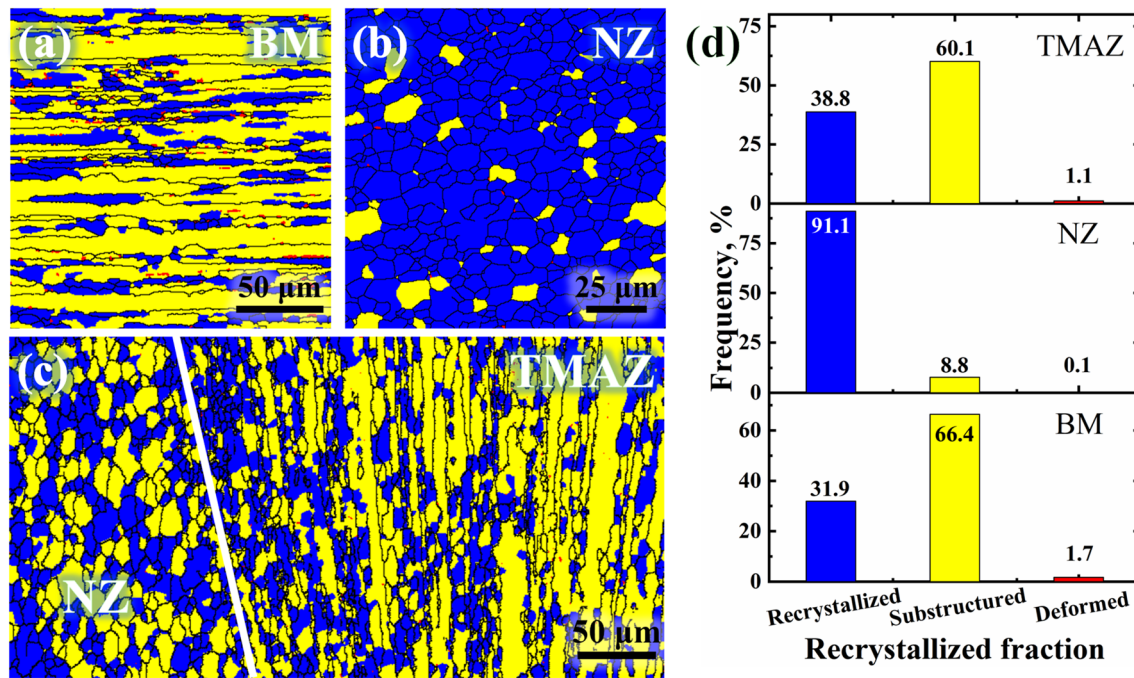


Fig. 7 Different grain types in **a** BM, **b** NZ, **c** NZ-TMAZ, and **d** fractions

exhibiting misorientation angles between 2° and 15° , are displayed as white lines, whereas high angle grain boundaries (HAGBs), surpassing 15° , are identified as black lines.

In BM, elongated and pancake grains with 58.6% HAGBs are detected, predominantly presenting the (101) and (111) orientations, as shown in Fig. 6a. In NZ, the original elongated grains change to fine and equiaxed grains ($\sim 5.7 \mu\text{m}$) with development of 92.4% HAGBs and random orientation (Fig. 6b). These HAGBs, resulting from FSW, indicate sufficient DRX generation. However, some LAGBs persist in the NZ grains, signifying concurrent DRV and DRX processes. In TMAZ, grains with elongated and layered shape are also found, but which are bent upward as response to material flow, as shown in Fig. 6c. The TMAZ mainly possesses

(001) orientation and 53.7% HAGBs. Fine recrystallization grains are also formed at the longitudinal direction of the elongated grains due to DRX formation.

Figure 7 displays the distribution and composition of different grain categories in BM, NZ, and TMAZ as identified by Channel 5 software. In the grain distribution maps, the red, yellow and blue denote deformed grains, sub-structured grains, and recrystallized grains, respectively. Sub-structured grains dominate in BM and TMAZ, while recrystallized grains are the maximum components in NZ. There is a notable rise in recrystallized grains from BM to TMAZ and NZ, escalating from 31.9% to 91.1%. BM presents the greatest proportion of sub-structured grains (66.4%) due to the rolling procedure. NZ displays not only the peak in

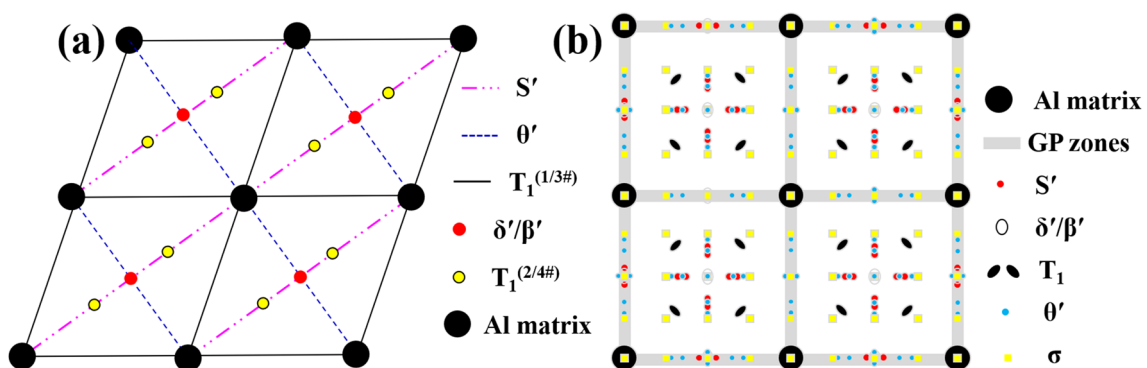


Fig. 8 Schematic SAED patterns of the precipitates in Al-Cu-Li alloy along **a** $[011]_{\text{Al}}$ and **b** $[001]_{\text{Al}}$ zone axes

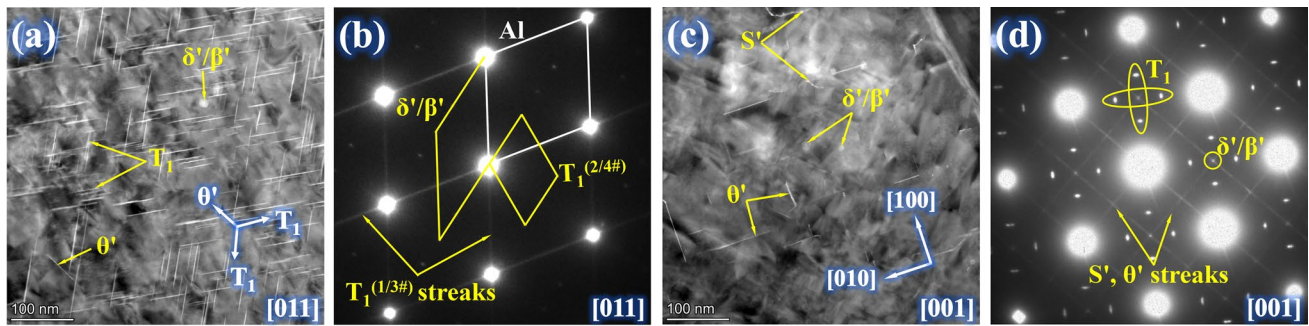


Fig. 9 STEM and SAED images of the BM along **a, b** $[011]_{\text{Al}}$ zone axis, and **c, d** $[001]_{\text{Al}}$ zone axis

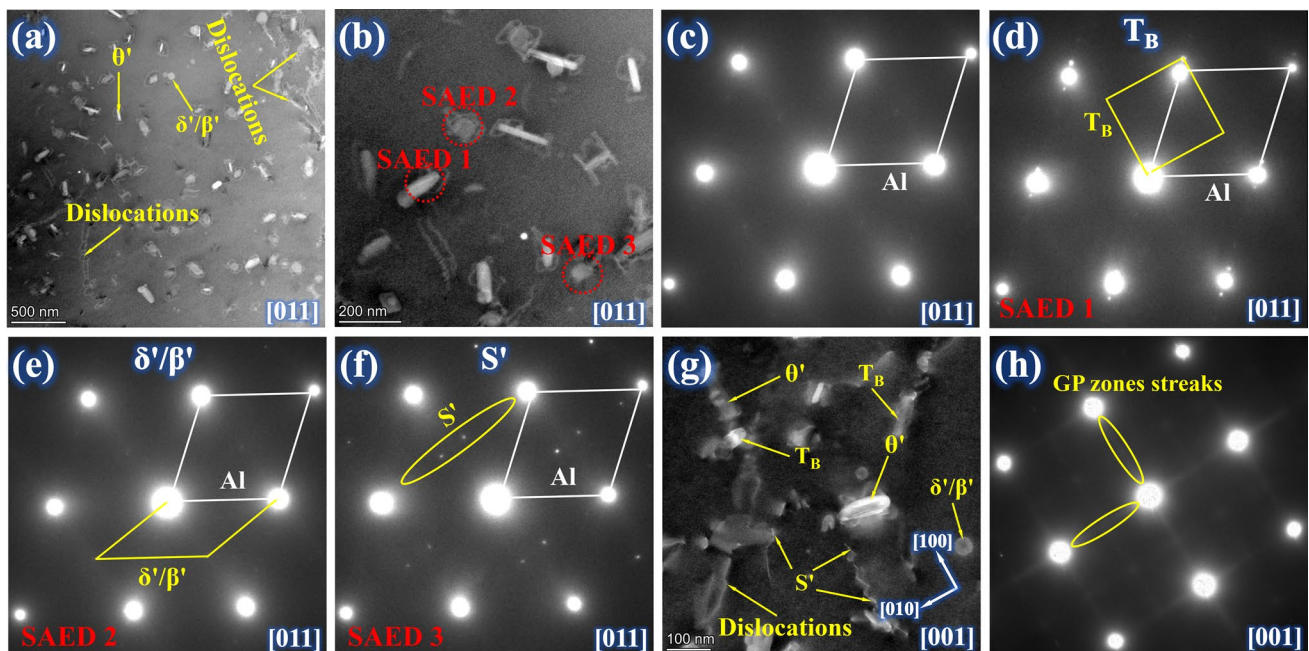


Fig. 10 STEM and SAED images of the NZ along **a–f** $[011]_{\text{Al}}$ zone axis, and **g, h** $[001]_{\text{Al}}$ zone axis. (**c** SAED corresponding to (**b**); **d** SAED of T_B ; **e** SAED of δ'/β' ; **f** SAED of S' ; **h** SAED corresponding to (**g**))

recrystallized grains (91.1%), but also the minimal fraction of deformed grains (0.1%) indicating comprehensive recrystallization. TMAZ exhibits sub-structured grains of 60.1% and recrystallized grains of 38.8%, displaying plastic deformation and partial dynamic recrystallization during welding.

3.3 Precipitates of the Joints

Al–Cu–Li alloy has a complex precipitation system and several kinds of precipitates. FSW is a kind of intricate thermo-mechanical process, which lead to complicated precipitate evolution in the individual regions of the joints. Thus, precipitates of BM, NZ, TMAZ, LHZ and HAZ are investigated by TEM under $[011]_{\text{Al}}$ and $[001]_{\text{Al}}$ zone axes, as shown in

Figs. 9, 10, 11, 12, 13, and 14. Figure 8 shows the schematic diagram of SAED patterns of the main precipitates in Al–Cu–Li alloy along $[011]_{\text{Al}}$ and $[001]_{\text{Al}}$ zone axes.

3.3.1 Precipitates of the BM

Figure 9 shows STEM and SAED images of the BM along $[011]_{\text{Al}}$ and $[001]_{\text{Al}}$ zone axes. When the incident electron beam aligns parallel to $[011]_{\text{Al}}$ zone axis, high density of T_1 possessing needle-like shape (about 50–120 in length and 2–5 nm in thickness) is viewed in the STEM images (Fig. 9a). This denotes the development of the 1# and 3# variants of T_1 ($T_1^{(1/3\#)}$). In the SAED images (Fig. 9b), not only the diffraction streaks for $T_1^{(1/3\#)}$, but also the

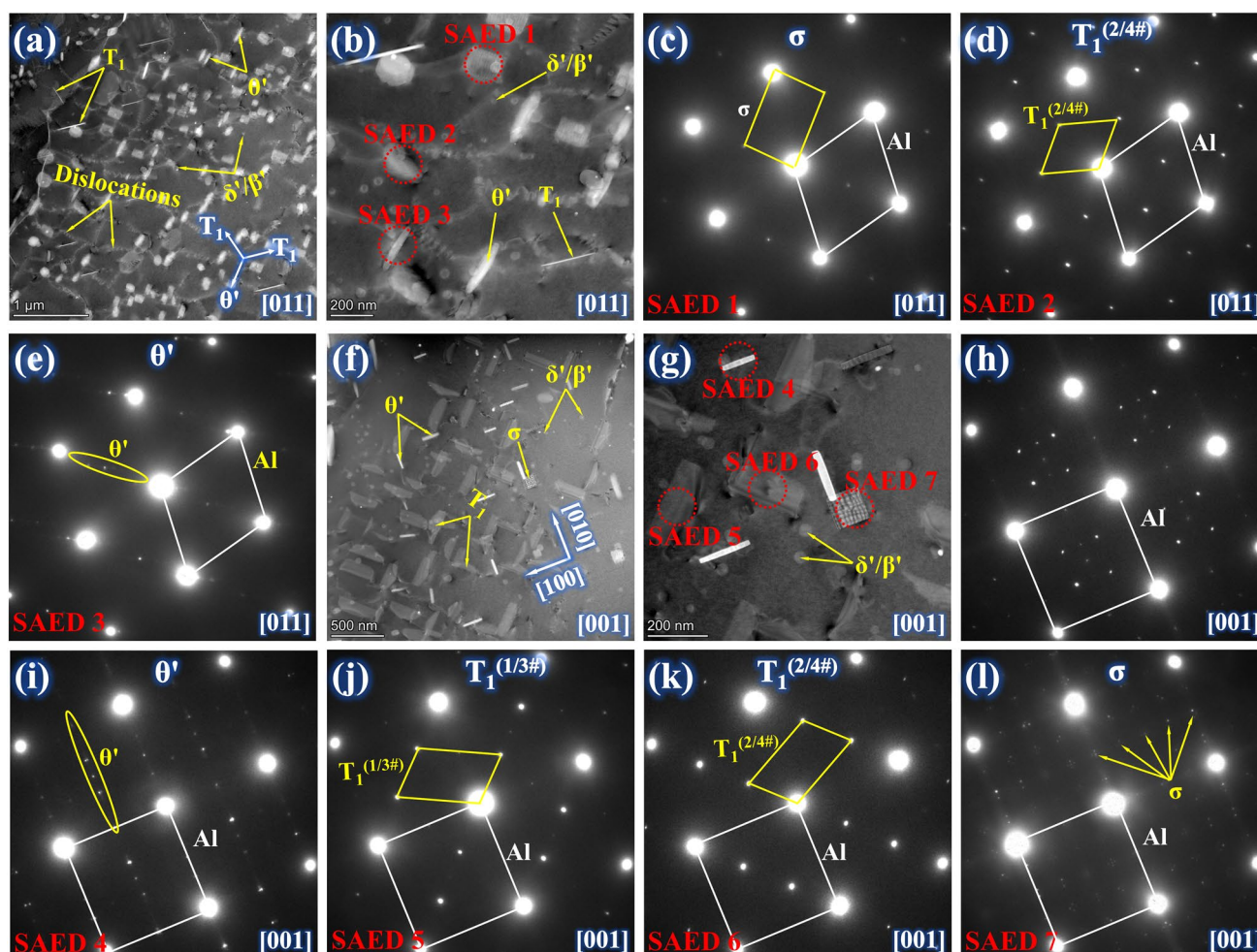


Fig. 11 STEM and SAED images of the TMAZ along **a–e** $[011]_{\text{Al}}$ zone axis, and **f–l** $[001]_{\text{Al}}$ zone axis. (**c, l** SAED of σ ; **d, k** SAED of $T_1^{(2/4\#)}$; **e, i** SAED of θ' ; **h** SAED corresponding to (**g**); **j** SAED of $T_1^{(1/3\#)}$)

diffraction spots corresponding to other two variants of T_1 ($T_1^{(2/4\#)}$) are also found, implying that four variants of T_1 exist in the BM. The δ'/β' precipitates are identified in the STEM and SAED images. The θ' is observed exhibiting a needle-like shape in STEM images, approximately 50–100 nm in length and 2–5 nm in thickness.

When the incident electron beam aligns with $[001]_{\text{Al}}$ zone axis, θ' , δ'/β' and S' are obviously viewed in the

STEM and SEAD images (Fig. 9c, d), while diffractions of T_1 with four variants are only detected in the SAED images (Fig. 9d). θ' displays two forms, perpendicular to one another, exhibiting needle-like morphology. δ'/β' demonstrate finely spherical shapes, measuring 10–30 nm. S' with lath shapes are mainly nucleated on helical dislocations. Consequently, T_1 , θ' , δ'/β' and S' are observed in

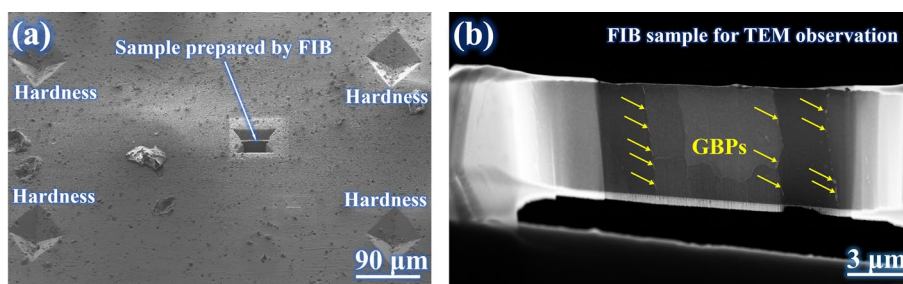


Fig. 12 Samples of the LHZ **a** prepared by combination of FIB and micro-hardness test, **b** observed by TEM

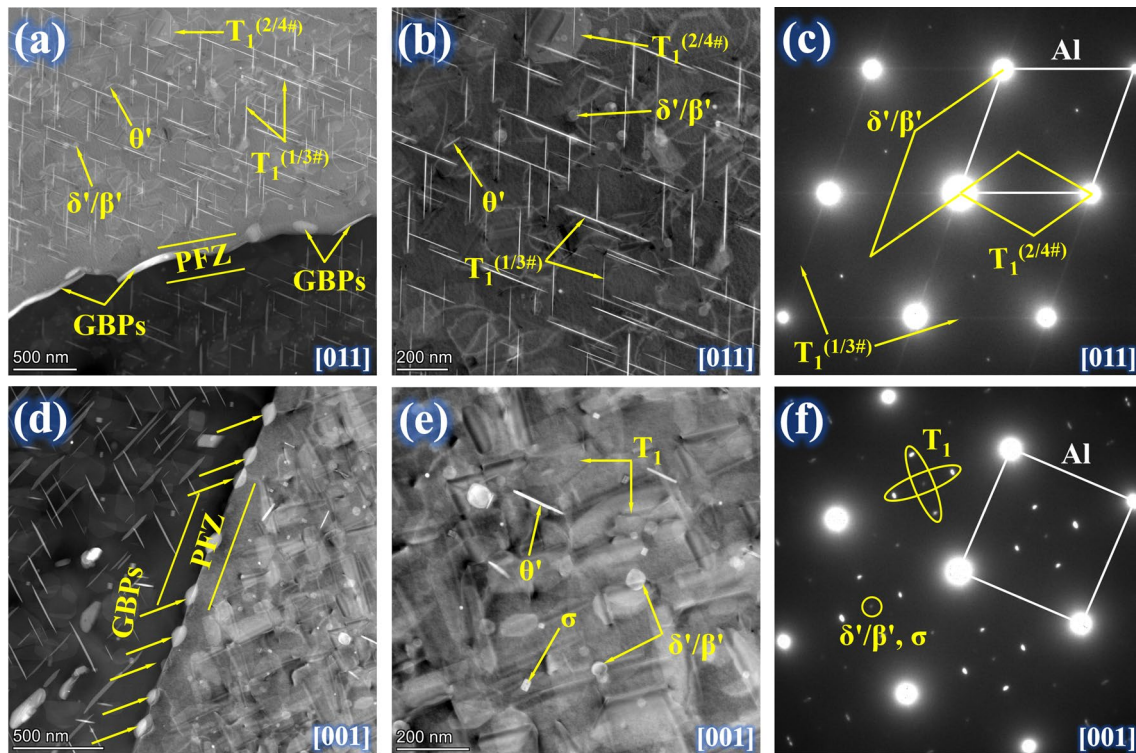


Fig. 13 STEM and SAED images of the LHZ along **a–c** $[011]_{\text{Al}}$ zone axis, and **d–f** $[001]_{\text{Al}}$ zone axis. (**c** SAED corresponding to (**b**); **f** SAED corresponding to (**e**))

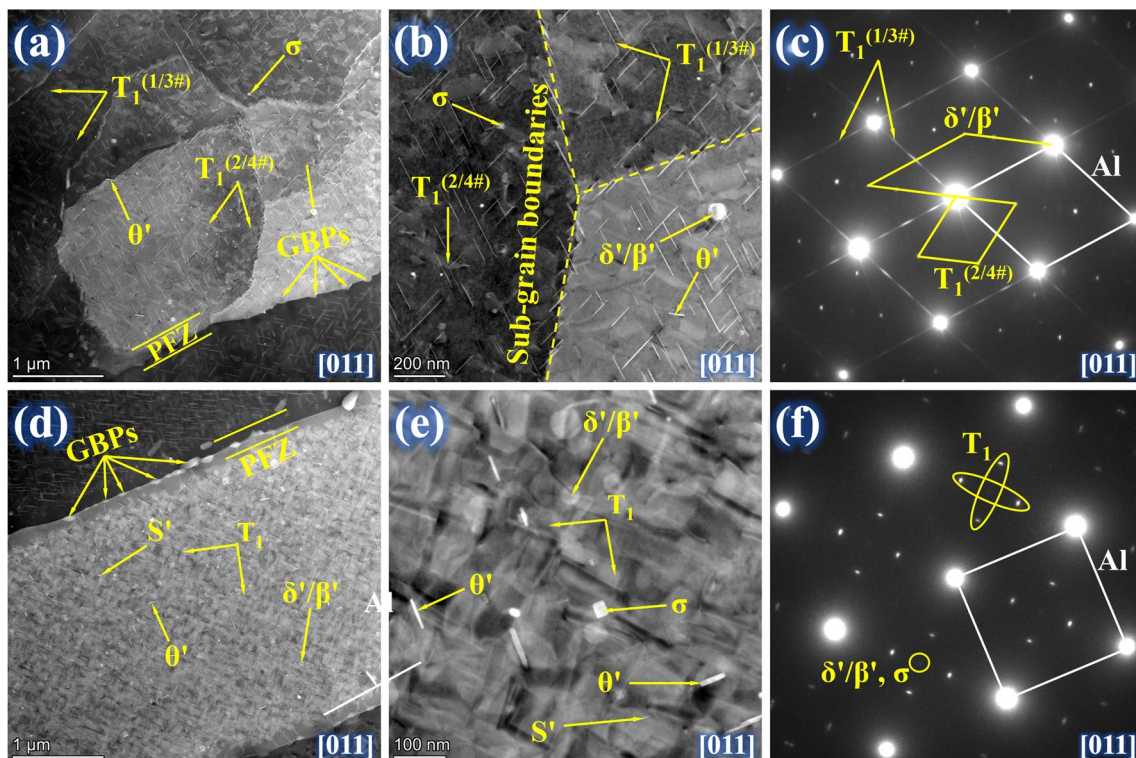


Fig. 14 STEM and SAED images of HAZ along **a–c** $[011]_{\text{Al}}$ zone axis, and **d–f** $[001]_{\text{Al}}$ zone axis. (**c** SAED corresponding to (**b**); **f** SAED corresponding to (**e**))

the BM, and T_1 is dominant in the temper conditions of this alloy.

3.3.2 Precipitates of the NZ

Figure 10 shows STEM and SAED images of the NZ along $[011]_{Al}$ and $[001]_{Al}$ zone axes. The NZ displays no remnants of the original T_1 in the STEM (Fig. 10a, g) or in SAED (Fig. 10c, h) images along these axes, suggesting complete precipitation dissolution. θ' , T_B , δ'/β' and S' are easily identifiable in the STEM images along the two diffraction axes, as shown in Fig. 10a, g. θ' grows to a bigger size. T_B is a kind of newly formed precipitate, which is identified by SAED analysis in Fig. 9d. Furthermore, this precipitate is exhibited a short rod-shape and always observed to be associated with a spherical precipitate along the two zone axes. It has been demonstrated that the spherical precipitate should be δ'/β' according to its morphology and diffraction spots (Fig. 9e). S' is identified by SAED analysis along $[011]_{Al}$ zone axis in Fig. 9f, and observed with irregular shapes in the STEM images. While, this precipitate is found with a rod shape and nucleated on dislocation along $[001]_{Al}$ zone axis, as shown in Fig. 10g. In addition, diffraction streaks corresponding to GP zones are detected in the SAED images along $[001]_{Al}$ zone axis. Consequently, complete dissolution of T_1 , growth of θ' , increase of δ'/β' and S' , and formation of GP zones and T_B occur in the NZ during the FSW.

3.3.3 Precipitates of the TMAZ

Figure 11 presents STEM and SAED images of the TMAZ, revealing a coarse T_1 , rather than the original fine precipitate, forming a total of four variants across the $[011]_{Al}$ and $[001]_{Al}$ zone axes. The needle-shape $T_1^{(1/3\#)}$ exhibits an apparent reduction in particle density with a size increase up to 200–400 nm in length and 8–15 nm in width, as shown in the STEM images along $[011]_{Al}$ zone axis (Fig. 11a). Figure 11d depicts the diffraction spots of the elliptical-shaped $T_1^{(2/4\#)}$, evident along the $[011]_{Al}$ zone axis. Furthermore, all four variants of T_1 exhibit elliptical features both in the STEM images and the SAED analysis along the $[001]_{Al}$ zone axis, as demonstrated in Fig. 11g, j and k.

θ' is evidently coarsened having 150–230 nm in length and 20–30 nm in diameter, which is viewed as a rod-shape in the STEM images along the two zone axes in Fig. 11b, f. Diffraction spots of θ' along the two directions are revealed in Fig. 11e, i. σ is a kind of newly developed precipitate and seen with a cubic shape in the STEM images along the two diffraction directions, as exhibited in Fig. 11a, f. Corresponding diffractions of σ are presented in Fig. 11c, l. S' disappears in the TMAZ, while δ'/β' are still observed in this region with content and size increasing. Besides, a lot of dislocations are viewed in this region. Thus, dissolution

and coarsening of T_1 , growth of θ' , formation of σ , dissolution of S' and increasing of δ'/β' occur in the TMAZ during the FSW.

3.3.4 Precipitates of the LHZ

The generation of LHZ is one of the typical features in FSW joints of precipitation strengthening Al alloys. According to the Fig. 5, LHZ is obviously located at the HAZ adjacent to the AS-TMAZ. As a narrow region (<0.5 mm) in the joints, the samples of LHZ for TEM observation are prepared combining FIB process and micro-hardness test, as represented in Fig. 12. This implies that location of the LHZ is determined by hardness analysis, and the sample is prepared by FIB.

Figure 13 displays STEM and SAED images of the LHZ along $[011]_{Al}$ and $[001]_{Al}$ zone axes. In the LHZ, four variants of T_1 can be clearly observed in the STEM images (Fig. 13b, e) and SAED images (Fig. 13c, f) along the two diffraction axes, indicating significant growth of this precipitate. The needle-shape $T_1^{(1/3\#)}$ observed along $[011]_{Al}$ zone axis (Fig. 13a) has 50–370 nm in length and 2–10 nm in thickness, as shown in Fig. 9a, b. Evidently, the size of this precipitate is larger but lower in the LHZ than in the BM (as displayed in Fig. 9a), signifying simultaneous precipitate coarsening and dissolution during welding.

According to Fig. 13b, e, θ' is found with a bigger size. The newly formed σ is detected with a little size. δ'/β' are observed with size and content raising, while S' disappears in LHZ. In addition, grain boundary phases (GBPs) and precipitate-free zone (PFZ) are clearly viewed near grain boundaries, which deteriorate to the mechanical properties of LHZ. The PFZ is usually viewed with a width of 250 ± 40 nm. Therefore, dissolution and coarsening of T_1 , coarsening of θ' , dissolution of S' , increase of δ'/β' and formation of σ , GBPs and PFZ occur in the LHZ.

3.3.5 Precipitates of the HAZ

Figure 14 shows STEM and SAED images of the HAZ along $[011]_{Al}$ and $[001]_{Al}$ zone axes. In the HAZ, four variants of T_1 can be obviously found in the STEM images (Fig. 14b, e) and SAED images (Fig. 14c, f) along the two diffraction directions. The $T_1^{(1/3\#)}$ observed along $[011]_{Al}$ zone axis (Fig. 14a) has 50–300 nm in length and 2–8 nm in thickness, which is evidently bigger than that in BM, but smaller than the precipitate in LHZ. Intensity of $T_1^{(1/3\#)}$ distinctly diminishes in the HAZ when compared to BM.

According to Fig. 14b, e, coarsening of θ' , size and content increase of δ'/β' , and newly developed σ are obviously found in HAZ, indicating similar precipitate features to LHZ (Fig. 13b, e). The original precipitate of S' is still viewed in HAZ and grows to a rod shape. GBPs and PFZ

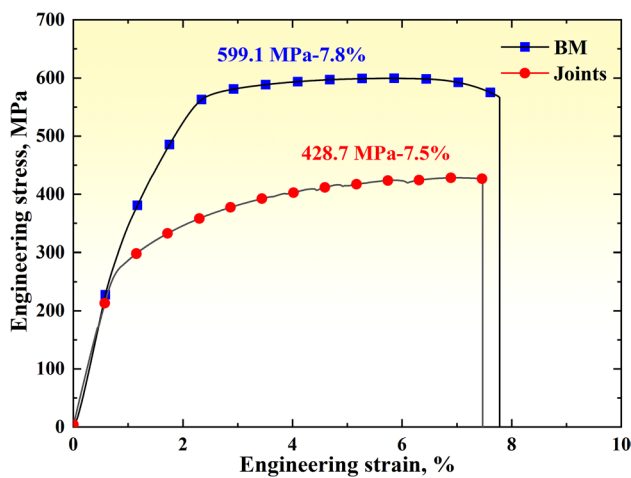


Fig. 15 Engineering stress–strain curves of BM and FSW joints

(200 ± 50 nm) are also found in this region. Hence, the HAZ has a similar precipitate evolution with the LHZ, which reveals that dissolution and coarsening of T_1 , coarsening of θ' and S' , increase of δ'/β' and formation of σ , GBPs and PFZ occur in the HAZ.

3.4 Tensile Properties of the Joints

Engineering stress–strain curves of the BM and FSW joints are exhibited in Fig. 15. The ultimate tensile strength (UTS) and elongation attained for the BM are 599.1 MPa and 7.8%, while those obtained for the FSW joints are 428.7 MPa and 7.5%. This implies that tensile properties of Al–Cu–Li alloys are diminished significantly post welding, resulting in a joint coefficient of 71.5%.

Tensile fracture occurs predominantly within the LHZ, with a fracture path at about 45° to the tensile axis. Fracture features of the BM and FSW joints are analyzed by SEM, as exhibited in Fig. 16. In the fracture surface of the BM, laminated cracks are generated along the boundaries of elongated grains, developing many large and smooth cleavage facets, as shown in Fig. 16a–c. In addition, small and shallow dimples with fine particles at the bottom are also observed, representing a few ductile fracture features. Therefore, cleavage fracture should be the dominant fracture mechanism for BM.

According to the fracture morphology of the joints (Fig. 16d–f), large intergranular cracks and cleavage facets are still viewed, indicating significant brittle fracture features. Furthermore, many micro-voids located along the laminated cracks are developed, as shown in Fig. 16d. These micro-voids are about 5–25 μm and always be filled with cracked particles (Figs. 15f and 16).

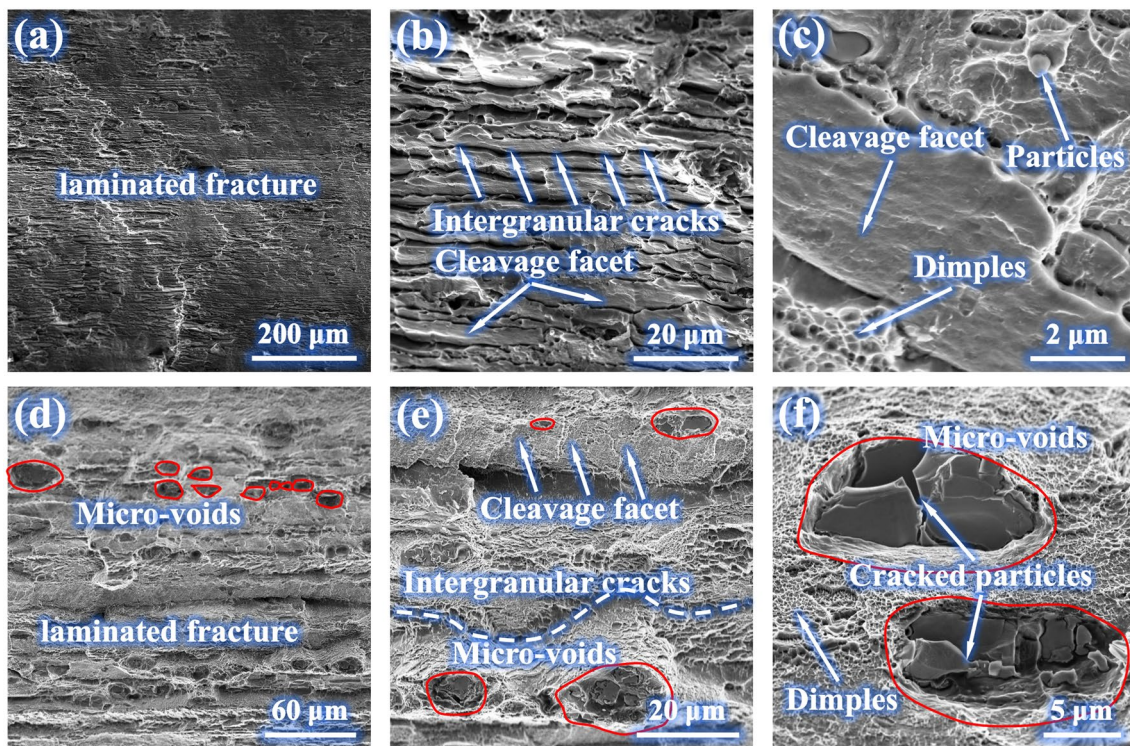


Fig. 16 Fracture morphologies of a–c BM and d–f FSW joints

4 Discussion

4.1 Evolution mechanism of grains

Rolling deformation creates elongated grains and pronounced dislocation density. During the artificial aging, the dislocations evolve to LAGBs by dislocation pile-up and dislocation annihilation leading to sub-grains forming. Thus, the BM contains LAGBs about 41.4% and sub-structure grains about 66.4%, as displayed in Figs. 6a and 7a.

During the FSW, HAZ is mainly affected by welding thermal cycle and undergoes recovery, resulting in little change in grain morphology and orientation. TMAZ is a transition zone between the HAZ and NZ, which is not directly stirred by rotating spin but extruded by NZ. Thus, this region suffers both mechanical and thermal effects, leading to grain rotation following material flow and elongated grains generating. Besides, partial DRX occurs in TMAZ due to the relatively low heat input, causing large sub-structured grains and a small number of recrystallized

grains developing (Fig. 7d). NZ is directly subjected to the stirring pin, undergoing severe plastic deformation and the maximum welding temperature. Both DRV and DRX take place in this region, and finally, finely equiaxed grains are formed due to the occurrence of complete recrystallization (Fig. 6b). Therefore, DRX occurs in NZ and TMAZ, and has different degrees in the two regions. To clarify DRX mechanism of NZ and TMAZ, enlarged observation of the grains is exhibited in Fig. 17.

According to Fig. 17a, recrystallization grains segmented by sub-grains are frequently observed in the NZ, indicating the generation of CDRX. Al alloy is a kind of high SPE material, and the dislocations are easy to slip and climb [14]. During the FSW, dislocations accumulate inside grains due to plastic deformation, resulting in many sub-grains generating. Furthermore, with the elevated strains and temperature, the dislocation motion leads to LAGBs progressively evolving to HAGBs and adjacent sub-grains merging to generate new grains. In addition, grains nucleated at triple junctions and the HAGB bulging to adjacent grains are also viewed, both of which are the typical features of DDRX. This implies

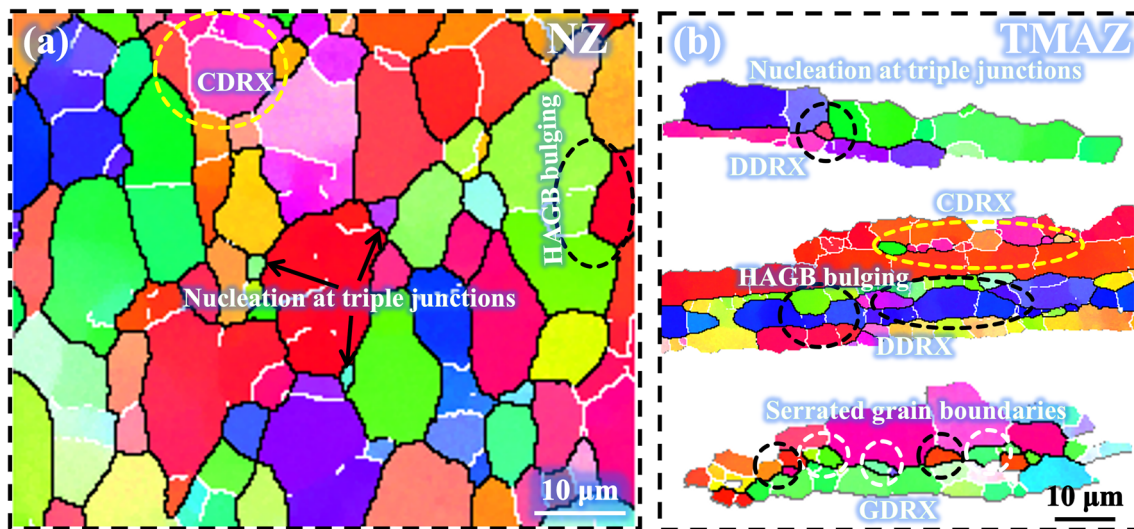


Fig. 17 Dynamic recrystallization in **a** NZ and **b** TMAZ

Table 2 Summary of precipitates in different regions of Al–Cu–Li alloy FSW joints

Regions	Precipitate evolution
BM	T_1 , θ' , δ'/β' and S'
NZ	T_1 completely dissolved, θ' dissolved and coarsened, δ' and S' reprecipitated, β' increased, GP zones and T_B newly formed
TMAZ	T_1 dominantly dissolved and the residual coarsened, θ' dissolved and coarsened, δ' reprecipitated, β' increased, S' dissolved, σ newly formed
LHZ	T_1 partially dissolved and the residual coarsened, θ' coarsened, δ' reprecipitated, β' increased, S' dissolved, σ , GBPs and PFZ newly formed
HAZ	T_1 partially dissolved and the residual coarsened, θ' and S' coarsened, δ' reprecipitated, β' increased, σ , GBPs and PFZ newly formed

that nucleation and growth of new grains are at the expense of dislocations formed during FSW. In TMAZ, CDRX and DDRX phenomena are obviously found, as revealed in Fig. 17b. Moreover, several finely equiaxed grains arrange along the boundaries of elongated grains which often have local serration-shaped boundaries and about 1–2 sub-grain size in width [13]. These features indicate that GDRX occurs in TMAZ. During FSW, the thermal–mechanical effect makes the serration-shaped HAGBs be being pinched off to develop new gains which always have a close orientation with the parent grains [14].

4.2 Evolution Mechanism of Precipitates

Precipitate evolution in Al–Cu–Li alloy FSW joint is summarized in Table 2. Al–Cu–Li alloy belongs to precipitation-strengthening Al alloys, whose mechanical properties are mainly determined by the type, content and size of precipitates [20]. Generally, dissolution, coarsening and precipitation of precipitates occur during FSW and have different degrees in individual regions of the joints, indicating diverse precipitation kinetics and precipitate distribution in these regions [2].

4.2.1 T_1 precipitate

The general precipitation process of Al–Cu–Li alloy is as follows [29]: supersaturated solid solution (SSSS) \rightarrow GP zones \rightarrow GP zones + δ' \rightarrow θ'' + θ' + δ' \rightarrow T_1 + δ' \rightarrow T_1 . Therefore, T_1 is the primary strengthening precipitate and supports high strength of this alloy. T_1 is detected in the BM with high density, small size and uniform distribution (Fig. 9a) due to the pre-deformation and peak artificial aging process, resulting in the high UTS (Fig. 15). Generally, peak temperature of the NZ is 0.6–0.9 T_m (T_m means the melting point of the BM), which can be calculated by the follows: $\frac{T}{T_m} = K \left(\frac{\omega^2}{v \times 10^4} \right)^\alpha$, where T is the maximum welding temperature, ω indicates rotation speeds, v represents welding speeds, K is a constant between 0.65–0.75, and α is another constant ranging from 0.04 to 0.06 [35]. It can be calculated that the peak temperature of NZ is about 429–494 °C in this study. It has been reported that dissolution temperature of T_1 is about 350 °C [29, 36]. Thus, the welding temperature of NZ is enough to promote T_1 dissolving into the matrix. It has also been demonstrated that precipitates of Al–Cu–Li alloy can be instantaneously driven into solution when the temperature is above 482 °C [37]. Hence, the original T_1 completely disappears in the NZ (Fig. 10), resulting from high welding temperature.

Peak temperature in TMAZ is lower than in NZ and usually obtained above 400 °C [38], resulting in the majority of T_1 dissolving into the matrix during the rapid welding process. It has been reported that exposure under 177–204 °C for a short time can make T_1 be evidently coarsened [36]. Hence, the residual T_1 in the TMAZ grows in a big size, even the four variants can be observed in the STEM images along $[011]_{Al}$ and $[001]_{Al}$ zone axes (Fig. 11). The maximum temperature of the HAZ is lower than that in TAMZ, and always above 350 °C [39]. In such case, HAZ has a similar T_1 evolution with TMAZ, but higher dissolution and coarsening degrees of T_1 are generated in TMAZ. LHZ is a transition region between the TMAZ and HAZ, which undergoes higher welding temperature than the other regions within the HAZ. This implies that less and coarser T_1 can be observed in the LHZ. Figure 18 shows the size distribution and number density of T_1 in the BM, LHZ and HAZ. It is obvious that BM develop the smallest size and highest number density of T_1 , while LHZ has the biggest size and least number density of T_1 .

4.2.2 θ' and GP zones

θ' is an important strengthening precipitate in 2xxxx Al alloys, which follows the classical precipitation sequence: SSSS \rightarrow GP zones \rightarrow θ'' \rightarrow θ' \rightarrow θ [40]. GP zones are localized concentrations of Cu atoms, and usually considered as a monolayer Cu platelet on $\{100\}_{Al}$ plane [28]. This structure is always developed by the solution heat treatment. FSW makes most of precipitates dissolve in NZ, and this process can be considered as a rapid solution treatment, resulting in the generation of GP zones. Consequently, the diffraction of GP zones can be viewed in NZ by SAED along $[001]_{Al}$ zone axis (Fig. 10h). The nucleation of θ' is at the expense of GP zones and θ'' (Al_2Cu), while in Al–Cu–Li alloy, this precipitate can be detected with T_1 sufficiently developing [41]. A few θ' observed in the BM is attributed to the adequate precipitation of T_1 during the artificial aging process. θ' can obviously coarsen and transform to the incoherent θ phase when prolonged exposure at 371 °C, and when above 427 °C, this precipitate will significantly diminish by dissolving in matrix [36]. Therefore, dissolution and coarsening of θ' mainly occur in NZ and TMAZ, while in HAZ as well as LHZ, θ' mostly take place coarsening, resulting from the lower welding heat input.

4.2.3 δ'/β' and S'

δ' and β' known as metastable precipitates are both easy to nucleate at low temperature due to low activation and interfacial energy [24]. δ' is a primary precipitate at 90–120 °C in Al–Li alloy, and evidently dissolved with the elevated

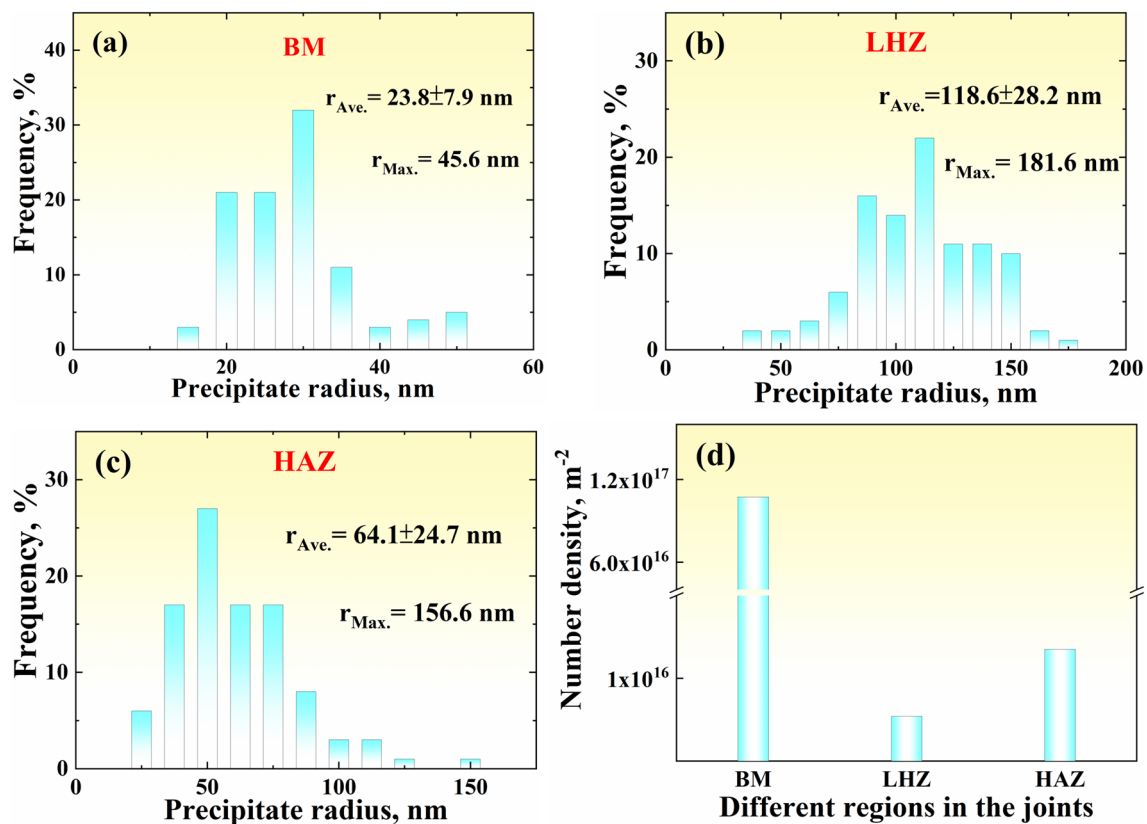


Fig. 18 Size distribution of T₁ in **a** BM, **b** LHZ and **c** HAZ, and **d** number density of T₁ in different regions of NZ

temperature [29]. As a result, during FSW, δ' mainly dissolves in the matrix due to the thermal effect at first, and then re-precipitates as well as grows in the cooling process. β' can act as nucleation sites for δ' precipitation and is often detected to be associated with δ' , while different with δ' , β' can be stable up to as high as 600 °C [26]. Thus, precipitation and coarsening of β' mostly occur in the FSW joints. The dissolution of T₁ increases the solute concentration and promotes δ' and β' generating further.

S' would prefer to nucleate on the edge of dislocations and always exhibits a lath morphology, while when the aging temperature is above 220 °C, this precipitate is mainly generated in a rod shape [26]. In NZ, S' initially dissolves due to the elevated temperature, subsequently reprecipitating owing to the thermal cycle. Rod-shaped S' is developed in this region resulting from the high heat exposure after welding. The production of θ' inhibits S' reprecipitating in TMAZ and LHZ due to competitive precipitation relationship, resulting in its disappearance in these regions. As relatively low welding temperature, S' majority coarsens in HAZ developing the rod-shaped precipitates.

4.2.4 σ and T_B

As the new precipitates generated in Al–Cu–Li alloy FSW joints, the cubic-shape σ and rod-shape T_B have been reported in other literatures [23, 33]. This analysis revealed that the cubic precipitate is primarily located in TMAZ, LHZ, and HAZ, while rod-shaped precipitates occur frequently in NZ. Ordinarily, σ known as Al₅Cu₆Mg₂ is an important strengthening precipitate in Al–Cu–Mg alloy [42]. This precipitate has about 46 at.% of Cu, which nucleation always needs a local scale of high concentration of Cu. The precise nucleation mechanism of σ is not clear, but the element Si and Ag and the weight Cu:Al ratio are considered as the important factors [25]. Despite no Si in BM, addition of silver stimulates precipitation of σ . Besides, Cu:Al ratio of the BM is about 10 which is higher than that in most of Al–Cu–Mg and play an important role in the precipitation of σ . T₁ dissolution augments matrix Cu content, stimulating σ nucleation during cooling. T_B preferentially nucleates on Si-rich particles linked to spherical β' dispersoids [23, 43]. In NZ, most of precipitates are dissolved allowing β' to develop and act as the nucleate sits for T_B generating.

4.2.5 GBPs and PFZ

GBPs and PFZ predominantly manifest in LHZ and HAZ, with formation attributed to thermal history. Above 315 °C, the precipitates θ , T_2 and T_B can form at grain boundaries, resulting in PFZ generating due to solute depletion [26]. With increasing temperature (> 350 °C), the equilibrium phases T_2 and T_B are significantly grown at the expense of θ , leading to the PFZ width improving [24]. Peak artificial aging promotes sufficient precipitation of solute atoms in BM, thereby treating LHZ and HAZ with high-temperature over-aging (about 280–390 °C) via FSW [39]. Consequently, GBPs and PFZs evolve in the both regions. With increasing temperature in LHZ, notably, GBPs and broader PFZ are formed. Generally, GBPs and PFZ allow localized dislocation motion (slip and climb), serving as stress concentrators potentially influencing void/crack initiation and propelling crack propagation along grain boundaries, enhancing early failure.

4.3 Mechanical Properties and Fracture Mechanism

Al–Cu–Li alloy belongs to precipitation-strengthening Al alloy, which mechanical properties mainly depend on precipitates. Notably, the dissolution and coarsening of T_1 are primarily responsible for reduced hardness and tensile strength. T_1 completely dissolves in the NZ, yet it does not generate the lowest hardness due to solid solution strengthening and fine grain strengthening. TMAZ also has a higher hardness than LHZ, owing to the dislocation strengthening and higher solid solution strengthening. The dissolution and coarsening degrees of T_1 is higher in LHZ than the other regions in HAZ, leading to the lowest hardness developing in the former. In addition, more GBPs and wider PFZ also play important roles to the maximum decrease of hardness in LHZ.

Tensile fracture occurs in the LHZ of Al–Cu–Li alloy FSW joints, which is a common phenomenon for the FSW joints of precipitation-strengthening Al alloys. To understand deformation behavior of the joints, strain distribution during continuous tensile deformation is analyzed by DIC. Representative strain distribution at varying tensile times is graphically illustrated in Fig. 19a where strain evenly distributes throughout the joints at the onset of 1 s due to low tensile stress. Subsequently, strain primarily accumulate at the HAZ under an escalating tensile stress, signifying heightened plastic deformation. By 100 s, locally intense strain concentration is discernible in the LHZ and subsequently results in joint failure within 5 s. Examination of joints deformed for 100 s reveals intruding precipitates in the LHZ as illustrated in Fig. 19b. Numerous cracked GBPs accompanying PFZ are evident, substantiating joint failure mechanisms. Thus, the failure mechanism can be depicted as the follows: (a) uniform deformation under low tensile stress resulting in elastic deformation; (b) with incremental stress, dislocations mobility accelerates, inducing local slip in the weak zones of the joints, particularly in the HAZ and LHZ; (c) stress concentration engenders near the GBPs and PFZ due to extensive plastic deformation in the LHZ, stimulating crack nucleation; (d) stress concentration intensifying, cracks and micro-voids progressively coalesce with adjacent ones, respectively, extending along grain boundaries until LHZ failure occurs. The micro-void coalesces and develops in a bigger size with cracked GBPs located at the bottom.

5 Conclusions

In this paper, microstructure and mechanical properties of Al–Cu–Li alloy FSW joints are studied. Evolution mechanisms of grains and precipitates are discussed in detail, and

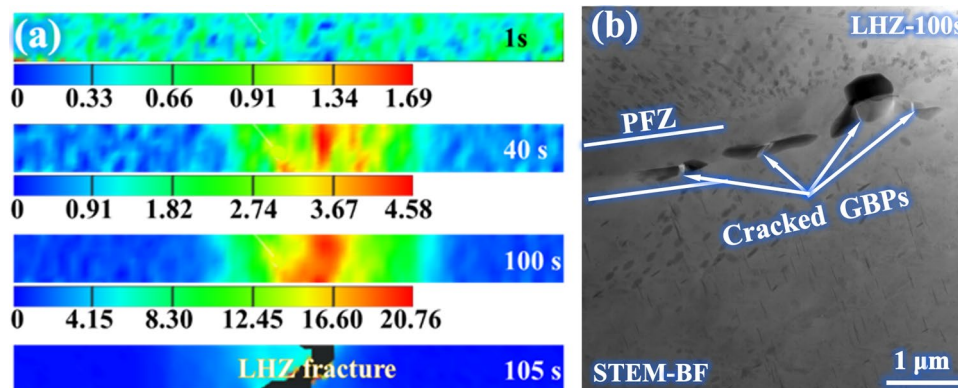


Fig. 19 **a** Macroscopic strain distribution contour of FSW joints at different tensile test time and **b** precipitate observation of LHZ when deformed by 100 s

the correlation of microstructure, mechanical properties and fracture mechanism of the joints are established. The main conclusions can be drawn as follows:

1. Finely equiaxed grains develop in NZ due to the complete DRX, and DDRX as well as CDRX are found in this region. A lot of sub-structured grains with elongated morphology are generated in TMAZ owing to the development of partial DRX, and DDRX, CDRX and GDRX are dominant in this region.
2. T_1 completely dissolves in the NZ, partially dissolves in TMAZ, LHZ and HAZ, where the residual T_1 is significantly coarsened leading to elliptical-shape $T_1^{(2/4\#)}$ generation. The dissolution and coarsening of θ' mainly occur in NZ and TMAZ, while in HAZ as well as the LHZ, θ' is primarily coarse. δ' dissolves in the matrix during the welding, re-precipitating and growing during cooling, while β' mainly experiences precipitation and coarsening. The lath S' firstly dissolves in NZ, and then reprecipitates with a rod-shape. Furthermore, this precipitate disappears in TMAZ and LHZ, but coarsens in HAZ.
3. σ , T_B , GBPs and PFZ are newly developed in the joints. σ is mainly found in TMAZ, LHZ and HAZ, while T_B is often observed in NZ. GBPs and PFZ are mostly developed in LHZ and HAZ.
4. The decline in the hardness and tensile strength of Al–Cu–Li alloy is chiefly due to the dissolution and coarsening of T_1 via FSW. The LHZ failure during tension indicates the involvement of GBPs and PFZ in crack initiation and progression.

Acknowledgements This research is financially supported by the Natural Science Foundation of Sichuan Province (2023NSFC0915), the Postdoctoral Research Project Special Fund of Sichuan Province and Natural Science Starting Project of SWPU (2023QHZ017).

Declarations

Conflict of interest The authors declare that they have no known competing financial interests or personal relationships that could have appeared to influence the work reported in this paper.

References

- [1] N. Eswara, A. Gokhale, R.J.H. Wanhill, *Aluminum–Lithium Alloys* (Elsevier, Butterworth-Heinemann, Kidlington, 2014), pp. 27–58
- [2] Y. Yang, J. Bi, H. Liu, Y. Li, M.Y. Li, S.S. Ao, Z. Luo, J. Manuf. Process. **82**, 230 (2022)
- [3] T. Jiang, T. Jiao, G. Dai, Z.K. Shen, Y.H. Guo, Z.G. Sun, W.Y. Li, J. Alloy. Compd. **935**, 168019 (2023)
- [4] N. Eswara, A. Gokhale, R.J.H. Wanhill, *Aluminum–Lithium Alloys* (Elsevier, Butterworth-Heinemann, Kidlington, 2014), pp.503–535

- [5] R. Mishra, H. Sidhar, *Friction Stir Welding of 2xxx Aluminum Alloys including Al–Li Alloys*, 1st edn. (Elsevier, USA, 2016)
- [6] M.N. Avettand-Fènoël, R. Taillard, J. Laye, O. Odièvre, Metall. Mater. Trans. A **4**, 5563 (2013)
- [7] Y.L. Ma, H.B. Xu, Z.Y. Yuan, L. Liu, Acta Metall. Sin. -Engl. Lett. **33**, 127 (2020)
- [8] M.M. Attallah, H.G. Salem, Mater. Sci. Eng. A **391**, 51 (2005)
- [9] H.S. Lee, J.H. Yoon, J.T. Yoo, K. No, Proc. Eng. **149**, 62 (2016)
- [10] J. Zhang, X.S. Feng, J.S. Gao, H. Huang, Z.Q. Ma, L.J. Guo, J. Mater. Sci. Technol. **34**, 219 (2018)
- [11] Y.Q. Mao, P. Yang, L.M. Ke, Y. Xu, Y.H. Chen, Acta Metall. Sin. -Engl. Lett. **35**, 745 (2022)
- [12] T.S. Liu, F. Qiu, H.Y. Yang, S.L. Shu, J.F. Xie, Q.C. Jiang, L.C. Zhang, Mater. Sci. Eng. A **871**, 144929 (2023)
- [13] D. Li, H. Liu, S. Du, X.M. Li, Y.S. Gao, Y.Y. Zuo, Mater. Sci. Eng. A **864**, 144572 (2023)
- [14] K. Huang, R.E. Logé, Mater. Des. **111**, 548 (2016)
- [15] Z. Shen, S. Chen, L. Cui, D. Li, X. Liu, W. Hou, H. Chen, Z. Sun, W.Y. Li, Mater. Charact. **186**, 111808 (2022)
- [16] P. Chen, J. Chen, S.Y. Qin, S.Q. Zou, S.B. Song, T. Jiang, Z.Q. Zhang, Z.H. Jia, Q. Liu, Mater. Sci. Eng. A **823**, 141501 (2021)
- [17] P. Chen, S.Q. Zou, J. Chen, S.Y. Qin, Q.B. Yang, Z.Q. Zhang, Z.H. Jia, L. Zhang, T. Jiang, Q. Liu, Mater. Charact. **176**, 111079 (2021)
- [18] P. Chen, T.N. Li, X. Yin, Y. Tang, G. Liu, S.B. Wang, B.S. Huang, Z.Q. Zhang, J. Mater. Res. Technol. **24**, 1991 (2023)
- [19] H. Sidhar, R.S. Mishra, Mater. Des. **110**, 60 (2016)
- [20] Z. Yu, J. Qiu, H. Li, P. Cai, L. Zhang, X.X. Fu, J.S. Wang, N.M. Xiao, Mater. Sci. Eng. A **863**, 144525 (2023)
- [21] M.X. Milagre, N.V. Mogili, U. Donatus, R.A.R. Giorjao, M.S. Terada, J.V.S. Araujo, C.S.C. Machacho, I. Costa, Mater. Charact. **140**, 233 (2018)
- [22] Y. Tao, Z. Zhang, B.H. Yu, P. Xue, D.R. Ni, B.L. Xiao, Z.Y. Ma, Mater. Charact. **168**, 110524 (2020)
- [23] R.W. Fonda, J.F. Bingert, Metall. Mater. Trans. A **37**, 3593 (2006)
- [24] N. Eswara, A. Gokhale, R.J.H. Wanhill, *Aluminum–Lithium Alloys* (Elsevier, Butterworth-Heinemann, Kidlington, 2014), pp.61–97
- [25] G.H. Wu, C.C. Shi, L. Zhang, W.C. Liu, A.T. Chen, W.J. Ding, Acta Metall. Sin. -Engl. Lett. **33**, 1243 (2020)
- [26] N. Eswara, A. Gokhale, R.J.H. Wanhill, *Aluminum–Lithium Alloys* (Elsevier, Butterworth-Heinemann, Kidlington, 2014), pp.99–137
- [27] C.H. Fan, L. Ou, Z.Y. Hu, S. Wang, J.H. Wang, Trans. Nonferrous Metal. Soc. **30**, 2590 (2020)
- [28] C. Liu, Z. Ma, P. Ma, L.H. Zhan, M.H. Huang, Mater. Sci. Eng. A **733**, 28 (2018)
- [29] J.H. Kim, J.H. Jeun, H.J. Chun, Y.R. Lee, J.T. Yoo, J.H. Yoon, H.S. Lee, J. Alloy. Compd. **669**, 187 (2016)
- [30] V.A. Peters, B. Gault, F.D. Geuser, A. Deschamps, J.L.M. Cairney, Acta Mater. **66**, 199 (2014)
- [31] T.F. Chung, Y.L. Yang, C.N. Hsiao, W.C. Li, B.M. Huang, C.S. Tsao, Z.S. Shi, J.G. Lin, P.E. Fischione, T. Ohmura, J.R. Yang, Inter. J. Lightw. Mater. Manuf. **1**, 142 (2018)
- [32] X.Y. Wang, J.T. Jiang, G.A. Li, X.M. Wang, J. Sun, L. Zhen, J. Alloy. Compd. **815**, 152469 (2020)
- [33] B. Cai, Z.Q. Zheng, D.Q. He, S.C. Li, H.P. Li, J. Alloy. Compd. **649**, 19 (2015)
- [34] Z.Y. Ma, A.H. Feng, D.L. Chen, J. Shen, Crit. Rev. Solid State **43**, 269 (2017)
- [35] R.S. Mishra, Z.Y. Ma, Mater. Sci. Eng. R **50**, 1 (2005)
- [36] P.S. Chen, B.N. Bhat, NASA Technical Report 211548 (2002).
- [37] J.A. Schneider, A.C. Nunes, P.S. Chen, G. Steele, J. Mater. Sci. **40**, 4341 (2005)
- [38] Y. Ni, Y. Liu, P. Zhang, J.K. Huang, X.Q. Yu, Mater. Charact. **187**, 11873 (2022)
- [39] J. Kang, M. Si, J. Wang, L. Zhou, X.D. Jiao, Q.P. Wu, Mater. Charact. **196**, 112634 (2023)

- [40] L. Zhou, C.L. Wu, P. Xie, F.J. Niu, W.Q. Ming, K. Du, J.H. Chen, *J. Mater. Sci. Technol.* **75**, 126 (2021)
- [41] Z. Shen, Q. Ding, C. Liu, J.W. Wang, H. Tian, J.X. Li, Z. Zhang, *J. Mater. Sci. Technol.* **33**, 1159 (2017)
- [42] H. Li, Y. Tang, Z. Zeng, Z.Q. Zheng, F. Zheng, *Mater. Sci. Eng. A* **498**, 314 (2008)
- [43] J.E. Kertz, P.I. Gouma, R.G. Buchheit, *Metall. Mater. Trans. A* **32**, 2561 (2001)

Springer Nature or its licensor (e.g. a society or other partner) holds exclusive rights to this article under a publishing agreement with the author(s) or other rightsholder(s); author self-archiving of the accepted manuscript version of this article is solely governed by the terms of such publishing agreement and applicable law.